2D and 3D Subsurface Resistivity Imaging Using a Constrained Least-Squares Algorithm

Manel Gasulla, Josep Jordana and Ramón Pallás-Areny

Divisió d'Instrumentació i Bioenginyeria, Departament d'Enginyeria Electrònica
Universitat Politècnica de Catalunya
Jordi Girona 1-3, Edifici C-4
08034 Barcelona, SPAIN
Phone 34-93-401-7483 Fax 34-93-401-6756
e-mail: mgasulla@eel.upc.es

Abstract - *This work describes a single-step constrained least-squares algorithm able to image underground electrical resistivity distributions. Using an approximate analytical solution for a spherical object embedded in a homogeneous medium yields synthetic data. A 16-electrode array yields 104 independent measurements. Shifting the electrode array parallel to itself permits us to obtain 3D images. The image reconstruction algorithm needs to calculate a damping factor in order to obtain a useful image. The L-curve method calculates a suitable damping factor automatically. However, an experimental trial-and-error refinement improves the accuracy in target detection.*

Experimental measurements involving spherical and cylindrical objects immersed in a water tank validate the proposed algorithm. Images deteriorate for deeper targets, particularly for spherical objects. Cylindrical objects whose axis is perpendicular to the electrode array are described by a 2D cross section, which need a reduced number of voltage measurements. Taking a reference measurement before immersing the objects in the water tank reduces errors in the reconstructed image because of the uncertainty in electrode positioning and the finite dimensions of the tank.

A field survey carried out on a farm field has permitted us to detect a 1 m plastic tube 16 cm in diameter, buried at 24 cm depth. The reconstruction algorithm is fast because it is non-iterative and takes only a few seconds to image the subsurface on a portable personal computer.

Keywords: Subsurface resistivity imaging, Least-squares algorithm, Electrical resitance tomography, Spherical and cylindrical targets.

1. INTRODUCTION

Geophysical prospecting often uses electrical resistance measurements aiming to detect buried objects and structures because of their resistivity contrast with the surrounding medium. Geoelectrical prospecting uses an electrode pair for current injection and a different electrode pair to measure the resulting drop in voltage, which depends on the injected current, electrode distance and underground resistivity distribution. This technique has proven its usefulness in soil contamination monitoring, in archaeological prospecting [1] and in shallow subsurface investigations, especially for groundwater studies [2].

Research on the interpretation of electrical soundings to determine the thickness and resistivity of layered media dates from the beginning of this century. A recent tendency is to image cross sections of underground resistivity distributions. One method for 2D subsurface imaging uses weighted backprojection, which derives mostly from medical imaging [3,4]. Noel and Xu [1] and Tsourlos et al. [5] have applied it to geoelectrical prospecting. However, most subsurface imaging techniques use the least-squares method. Loke and Barker [6] use a smoothness–constrained least-squares method to achieve a smooth solution. Backprojection and least-squares methods can both be implemented as single-step or iterative algorithms.

Iterative methods calculate the sensitivity matrix and surface potentials at each iteration using some numerical methods (finite elements, difference elements), which is computation-intensive. This problem worsens for 3D imaging because of the increased number of data and parameters. Some authors have proposed techniques suited to reduce computation time [7, 8]. Nevertheless, iterative algorithms have

convergence problems and may not achieve a correct solution.

Gasulla et al. [9] compare two 2D single-step algorithms based, respectively, on the sensitivity weighted-backprojection method and a constrained least-squares method. This last is more accurate in locating objects and their conductivity, and its results are relative insensitive to he object's depth. This work describes a least-squares algorithm based on the Marquardt-Levenburg method [10] to obtain 2D and 3D conductivity images.

2. PROBLEM STATEMENT

Geoelectric prospecting involves a large number of measurements, particularly for 3D imaging. Manually switching the injecting and detecting electrodes at each measurement is time-consuming and tedious. Gasulla et al. [11] describe two automated systems to speed the measurement process that allow us to select any pair from a 16-electrode array for current injection and voltage detection. In [9] the same authors describe two arrays that use 16 uniformly-spaced electrodes and derive from the Schlumberger and dipole-dipole arrays. Because of the larger relative errors for the dipole-dipole array, it will not be considered here.

The current-injecting electrode pairs for the modified Schlumberger array in [9] are (1, 16), (2, 16) and so on until (13, 16). For each current pair, we measure the differential voltage between successive pairs of adjacent electrodes placed between the injecting electrodes, which yields 91 voltages. However, using 16 electrodes yields 104 independent measurements [1]. The remaining 13 measurements result from injecting by electrode pair (1,15) and detecting voltage between pairs of inner electrodes —12 measurements— and injecting by electrode pair (3, 16) and detecting the drop in voltage across electrode pair (1,2). The imaged section lies beneath the electrode array. Figure 1. shows a cross section divided into 5 layers of 16 pixels each. Shifting the electrode array parallel to itself along the y axis yields 3D images. The origin of coordinate axis is centered between electrodes 8 and 9.

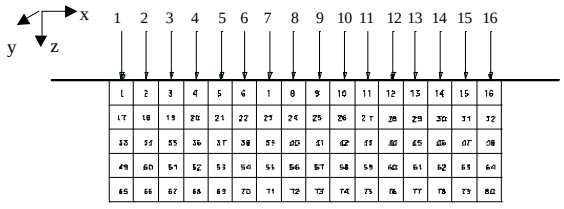

Figure 1: 2D subsurface model and 16-electrode array with uniformly spaced electrodes.

We have imaged subsurface conductivity distributions using a least-squares algorithm based upon the Marquardt–Levenburg method,

$$\boldsymbol{s}^{est} - \boldsymbol{s}^{o} = \left(S^t S + \boldsymbol{l} I\right)^{-1} S^t \left(Z - Z^o\right) \qquad (1)$$

where: σ^{est} is the estimated conductivity vector; σ^o is the initial (model) conductivity vector; Z is the mutual impedance vector [12], whose elements are the measured differential voltages divided by the current injected; Z^o is the mutual impedance vector calculated for a conductivity distribution σ^o; S is the Jacobian or sensitivity matrix; S^t is the trasposed of S; I is the identity matrix; and λ is a damping factor. Choosing a homogeneous σ^o permits us to analytically calculate Z^o and to obtain S simply [4,6]. Further more, calculating S beforehand and storing it saves computation time.

The following sections discuss results obtained by the above algorithm when using synthetic data, data from resistivity measurements in a laboratory water tank, and field measurements.

3. SYNTHETIC-DATA IMAGES

Classical solutions for electric potential distributions are useful in geophysical prospecting because allow us to estimate the relative influence of different geometric and physical parameters of the target, such as size, depth and resistivity. An analytic mathematical solution yields a fast, accurate and inexpensive set of voltages for a given target.

Wait [13] offers an analytical solution for the voltage distribution resulting from a point current injection in a homogeneous medium including a spherical object. Telford et al. [14] consider the effect of the ground–air interface. Figure 2. shows the parameters when there are two point electrodes for current injection.

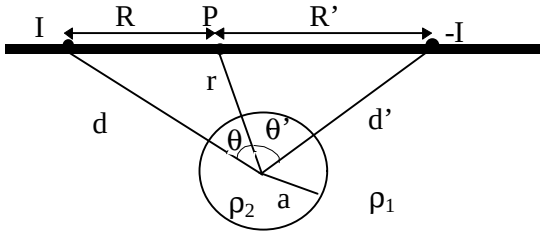

Figure 2: Spherical object, injecting electrodes and measurement point (P).

The approximate voltage at a point P on the surface is

$$V(P) = \frac{I\boldsymbol{r}_1}{2\boldsymbol{p}}\left(\frac{1}{R} - \frac{1}{R'}\right) + \frac{I\boldsymbol{r}_1}{2\boldsymbol{p}} \sum_{n=0}^{\infty} k_n \frac{a^{2n+1}}{r^{n+1}} \left(\frac{P_n(\cos\boldsymbol{q})}{d^{n+1}} - \frac{P_n(\cos\boldsymbol{q}')}{(d')^{n+1}}\right) \qquad (2)$$

where

$$k_n = 2\frac{n(\boldsymbol{r}_2 - \boldsymbol{r}_1)}{(n+1)\boldsymbol{r}_2 + n\boldsymbol{r}_1} \quad (3)$$

and P_n are Legendre's polynomials. The first term in (2) is the primary voltage because of the homogeneous medium, and the second term is the secondary voltage because of the added sphere.

Equation (2) yields the values for Z and Z^o needed in (1). We assume an homogeneous soil with conductivity 1 S/m, and a unity current injection (1 A). The are 16 electrodes uniformly spaced at unit distance along the x axis at $y = 0$. Let us first consider a unit-radio sphere with zero conductivity placed between electrodes 8 and 9 ($x = y = 0$) at two-units depth ($z = 2$). The particular damping factor $\boldsymbol{l}$ determined from the L-curve method [15] is 1.18×10^{-5}. Figure 3. shows images obtained for $\boldsymbol{l} = 1.18 \times 10^{-5}$, $\boldsymbol{l} = 1.18 \times 10^{-4}$ and $\boldsymbol{l} = 1.18 \times 10^{-3}$. The cross section has been divided in 16 × 1 x 5, each 1x2x1 units. Larger values for λ yield smoother images, reduce the estimated conductivity and assign it to shallow pixels. The target position is correctly detected.

a)

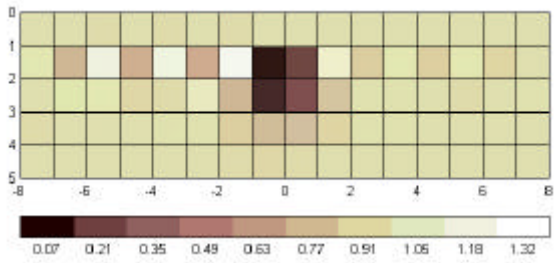

b)

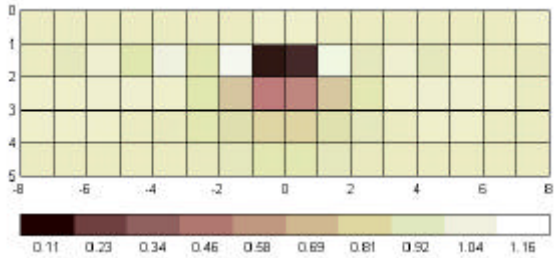

c)

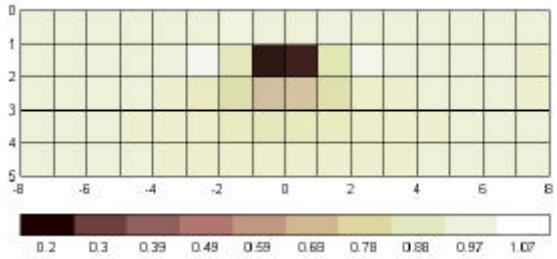

Figure 3: 2D images from a unit radio non-conductive sphere placed at $x = y = 0$, $z = 2$, for a) $\boldsymbol{l} = 1.18 \times 10^{-5}$, b) $\boldsymbol{l} = 1.18 \times 10^{-4}$, and c) $\boldsymbol{l} = 1.18 \times 10^{-3}$

Figures 4 and 5 show 2D images from, respectively, a sphere placed at $x = y = 0$, $z = 3$ and $x = 4$, $y = 0$, $z = 2$. When z = 3, $\boldsymbol{l} = 9.24 \times 10^{-9}$, hence quite smaller compared to that for $z = 2$.

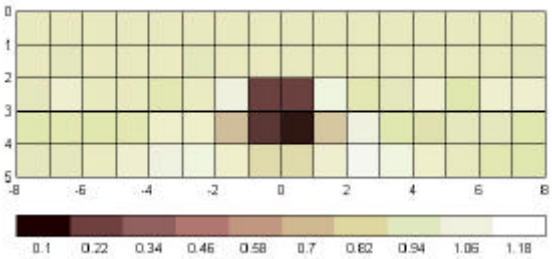

Figure 4: 2D image from a unit-radio non-conductive sphere placed at $x = y = 0$, $z = 3$ ($\boldsymbol{l} = 9.24 \times 10^{-9}$).

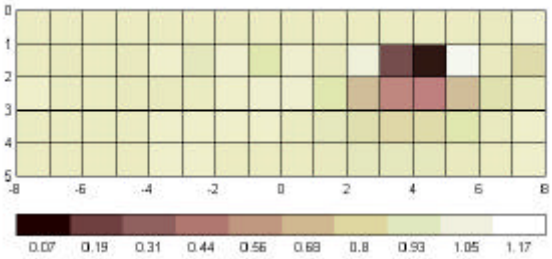

Figure 5: 2D image from a unit-radio non-conductive sphere placed at $x = 4$, $y = 0$, $z = 2$ ($\boldsymbol{l} = 7.36 \times 10^{-5}$).

Figure 6. shows the image for a unit-radio, perfectly conductive sphere placed at $x = y = 0$, $z = 2$. The maximal conductivity change detected is 1.69, almost twice and with sign opposite to that for a non-conductive sphere. This is in agreement with the fact that the secondary potential in (2) when current injecting electrodes are far away is almost twice and has opposite sign for a conductive sphere compared to a non-conductive sphere.

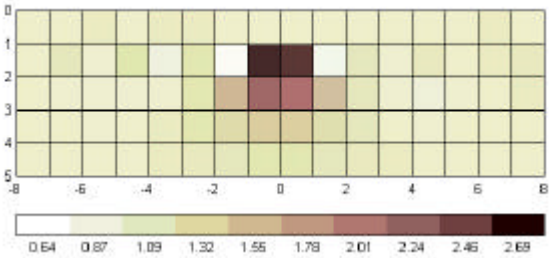

Figure 6: 2D image from a unit-radio conductive sphere placed at $x = y = 0$, $z = 2$ ($\boldsymbol{l} = 1.04 \times 10^{-4}$).

Nevertheless, 2D images may lead to equivocal results when the sphere is not in the same plane as the electrode array. For example, Figure 7 shows the image from a unit-radio non-conductive sphere placed at $x = 0$, $y = 2.24$, $z = 2$. The image looks similar to that in Figure 4, i.e., the detected depth is 3 (distance from the electrode array) instead of 2 (actual depth).

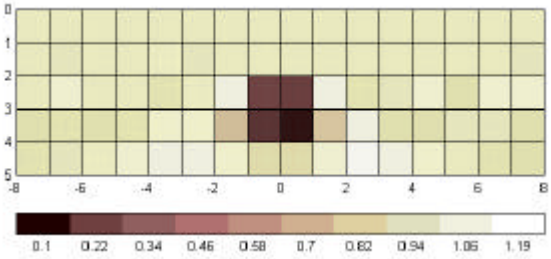

Figure 7: 2D image from a unit-radio non-conductive sphere placed at $x = 0$, $y = 2.24$, $z = 2$ ($\boldsymbol{l} = 9.24 \times 10^{-9}$).

Reliable imaging underground conductivity distributions needs 3D images. In the above example, the electrode array successively placed at $y = 0$, $y = 2$ and $y = 4$, and the underlying volume is divided in $16 \times 3 \times 5$ voxels, each $1 \times 2 \times 1$ units. Figure 8. shows a vertical cross-section at $y = 2$ and a horizontal cross-section at $z = 1.5$. As opposed to the 2D image in Figure 7, the sphere is now correctly detected.

a)

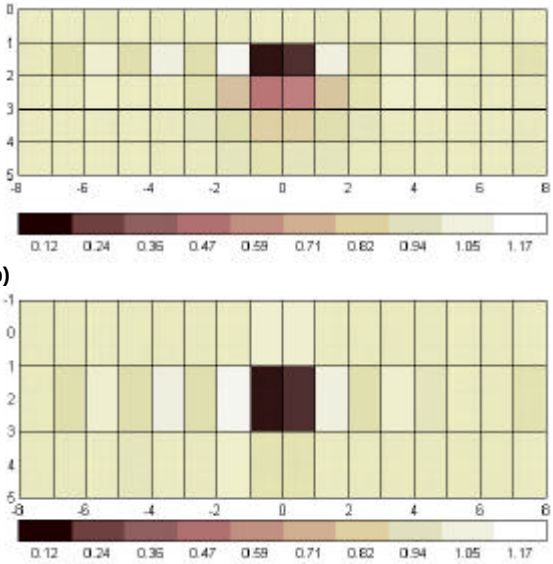

b)

Figure 8: 3D image of a unit-radio, non-conductive sphere placed at $x = 0$, $y = 2.24$, $z = 2$ ($\boldsymbol{l} = 8.37 \times 10^{-5}$). The volume beneath the electrode array has been divided in $16 \times 3 \times 5$ voxels measuring $1 \times 2 \times 1$ each. a) Vertical cross-section at $y = 2$, b) Horizontal cross-section at $z = 1.5$.

4. IMAGES FROM RESISTIVITY MEASUREMENTS IN A TANK

The reconstruction algorithm has been experimentally tested by imaging a rubber ball (2.2 cm in radius) and a PVC cylinder (25 cm long, 2 cm in radius) immersed into a plastic water tank (40 cm × 35 cm × 20 cm). The electrode array consisted of 16 electrodes spaced 2 cm. An automatic data acquisition system obtained the voltage data [11]. The effects of the tank's finite dimensions are partially cancelled by calculating Z^0 in (1) from voltage measurements taken without any immersed object and then dividing (1) by Z^0.

Figure 9 and 10 show 2D images for the sphere at 2 cm depth (unit electrode spacing) when placed, respectively, at $x = y = 0$, and $x = 4$, $y = 0$ ($z = 2$ in both cases). The conductivities displayed are normalised to water conductivity (about 0.15 S/m). The detected conductivity change is larger than that in Figures 3 and 5, respectively, because the sphere radius is now 1.1 units instead of one unit.

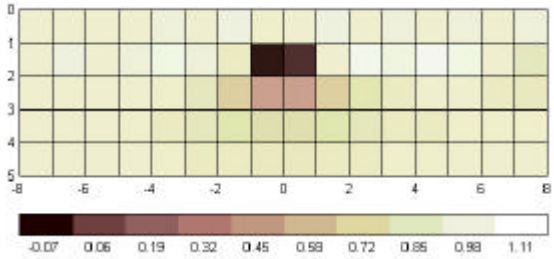

Figure 9: 2D image of a non-conductive sphere with 1.1 units radius placed at $x = y = 0$, $z = 2$ ($\boldsymbol{l} = 9.19 \times 10^{-4}$).

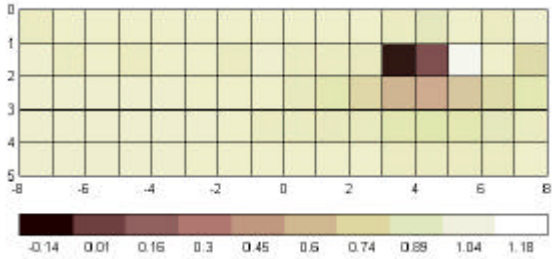

Figure 10: 2D image of a non-conductive sphere with 1.1 units radius placed at $x = 4$, $y = 0$, $z = 2$ ($\boldsymbol{l} = 2.23 \times 10^{-4}$).

Figure 11 shows the image for the sphere placed at $x = y = 0$, $z = 3$. The image deteriorates as compared to that in Figure 4, obtained from synthetic data. Deleterious effects arise from measurement inaccuracy, finite tank dimensions, and time drift of water conductivity because of temperature changes. These negative effects are augmented because of the deeper position of the rubber ball. In addition, the detected change in conductivity is smaller because it is attributed to more cells.

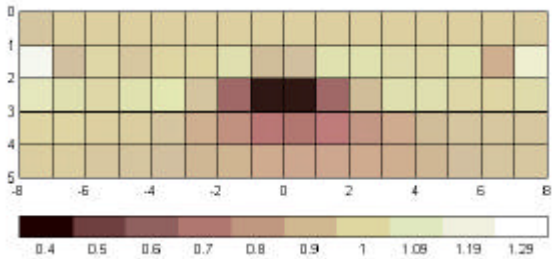

Figure 11: 2D image of a 1.1 units radius non-conductive sphere placed at $x = y = 0$, $z = 3$ ($\boldsymbol{l} = 3.78 \times 10^{-5}$).

A method to perform 3D measurements is to shift the electrode array along the *y* axis. This method is cumbersome and implies a different effect from tank walls for different measurements. A possible solution is to shift the sphere instead. We have measured voltage profiles when the sphere was placed at $x = 0$, $y = 0$, and then successively at $y = -2$, $y = -4$, and $y = -6$. This last measurement was used as reference (Z^0). The volume was divided in $16 \times 3 \times 5$ voxels measuring $1 \times 2 \times 1$ units. Figure 12 shows a vertical cross-section at $y = 0$ and a horizontal cross section at $z = 1.5$. The imaging process assumes that the sphere stays in place and the electrode array shifts along the *y* axis. The position of the sphere is correctly detected.

a)

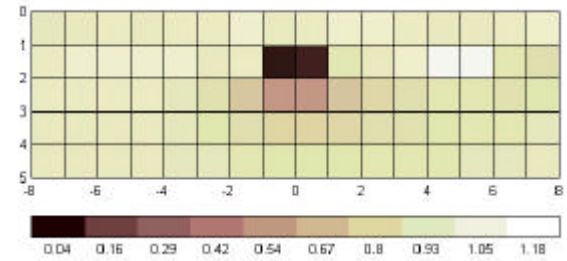

b)

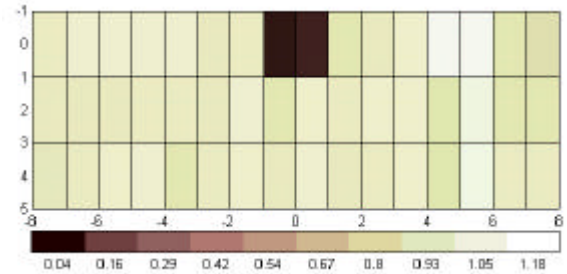

Figure 12: 3D image of a 1.1 units radio, non-conductive sphere placed at $x = y = 0$. Instead of displacing the electrode array, the sphere has been successively placed at $y = 0$, $y = -2$, and $y = -4$. The reference measurement is taken with the sphere placed at $y = -6$. The volume is divided in $16 \times 3 \times 5$ voxels measuring $1 \times 2 \times 1$ units. a) Vertical cross-section at $y = 0$. b) Horizontal cross section at $z = 1.5$. ($\sigma = 1.14 \times 10^{-3}$)

Cylinders model mine shafts, tunnels and pipes. Figure13 shows the 2D image of a PVC tube immersed 2 units beneath the electrode array in the water tank above described. In order to show that the tube is effectively beneath the electrode array we would need 3D measurements.

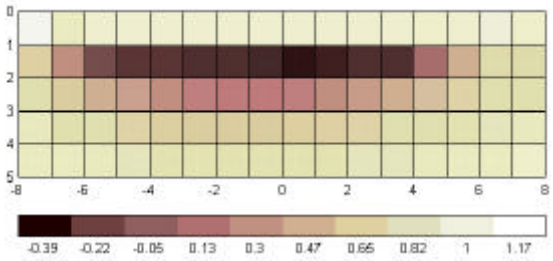

Figure 13: 2D image of a 1 unit radius, PVC cylinder, 12.5 units long, whose axis is at $y = 0$ and depth 2 units ($\sigma = 2.42 \times 10^{-3}$)

Targets with infinite dimension along a given axis are better modelled by voxels with infinite dimension along that axis. Loke and Barker [6] show how to calculate the sensitivity of each voxel. These targets do not require us to shift the electrode array, which saves both measurement and computation time. Figure 14 shows the image for a cylinder placed at $x = 0$, $z = 2$ with axis parallel to axis y. We have performed two measurement sets with the array placed at $y = 0$, one without the cylinder and the other with the cylinder in place.

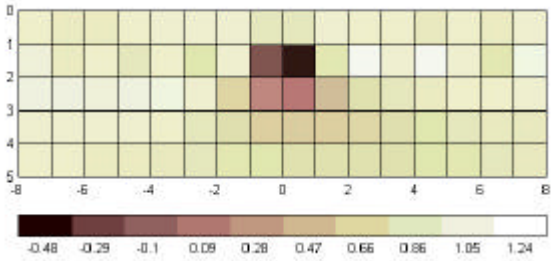

Figure 14: 2D image for a 1 unit radius PVC cylinder 12.5 units long with axis at $x = 0$ immersed 2 units in water ($\sigma = 8.80 \times 10^{-4}$)

Field measurements described in the next section use an eight-electrode system [16]. Figure 15 shows the 3D image obtained by that system when the rubber ball is immersed at $x = 0$, $y = 0$, $z = 2$. Electrode distance is 2 cm. The volume has been divided in $16 \times 2 \times 5$ voxels measuring $1 \times 2 \times 1$ units. The electrode array has been successively placed at y = 0.5, y = 1.5, y =2.5, and y = 3.5, which constitutes the reference measurement. Moving the array is now easier because there are only 8 electrodes and tank walls have a smaller effect.

a)

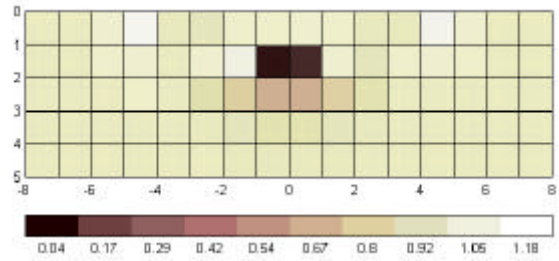

b)

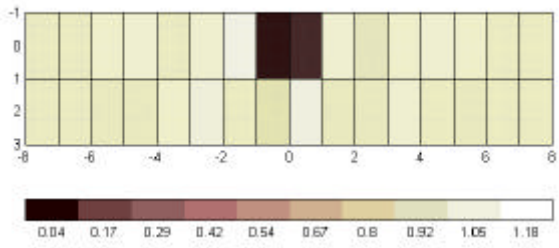

Figure 15: 3D image of a unit-radio, non-conductive sphere placed at $x = y = 0$, $z = 2$. The volume has been divided in $16 \times 2 \times 5$ voxels measuring $1 \times 2 \times 1$ units. Voltage measurements have been performed with an 8-electrode array placed successively at $y = .5$, $y = 1.5$, $y = 2.5$, and $y = 3.5$, which constitutes the reference measurement. a) Vertical cross-section at $y = 0$, b) Horizontal cross section at $z = 1,5$. ($I = 3.26 \times 10^{-5}$)

Figure 16 shows the 3D image for a 1 cm radius (0.5 units), 25 cm long (12.5 units) PVC cylinder whose axis was parallel to axis x and placed at $y = 0$, $z = 1.5$ units. The volume has been divided in $16 \times 2 \times 5$ voxels measuring $1 \times 2 \times 1$ units. Voltage measurements have been performed with an 8 electrode array successively placed at $y = .5$, $y = 1.5$, $y = 2.5$, and $y = 3.5$, which constitutes the reference measurement.

a)

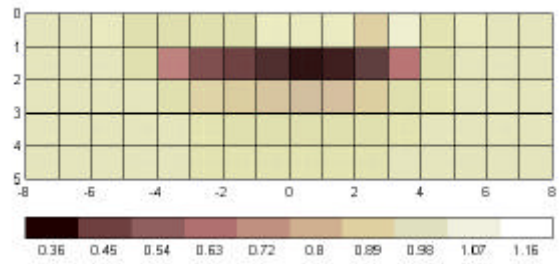

b)

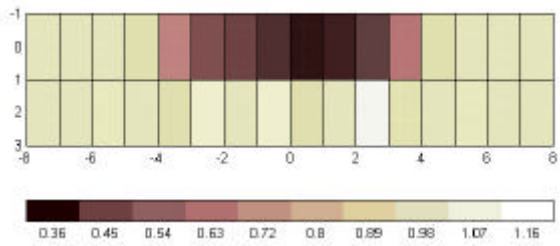

Figure 16: 3D image for a 0.5 units radius, PVC cylinder whose axis was parallel to axis x, immersed at $y = 0$, $z = 1.5$ units in a water tank. The volume is divided in $16 \times 2 \times 5$ voxels measuring $1 \times 2 \times 1$ units. Voltage measurements have been performed with an 8-electrode array successively placed at $y = .5$, $y = 1.5$, $y = 2.5$, and $y = 3.5$, which constitutes the reference measurement. a) Vertical cross-section at $y = 0$. b) Horizontal cross-section at $z = 1,5$. ($I = 6.97 \times 10^{-5}$)

5. IMAGES FROM FIELD MEASUREMENTS

Field measurements have been undertaken at a farmer filed in Sta. Eulalia de Ronçana (Barcelona, Spain). Figure 17 shows the measurement layout. The target was a 1.06 m long PVC tube 8 cm in radius, buried at 24 cm depth in the farm ground. The tube axis was parallel to x axis. The ground consisted of a 32 cm farm soil on a rocky layer tilted towards the west. On the south side of the buried tube there was an additional vertical plastic tube 7 cm in diameter used to inject water in order to simulate a water leak. (Figure 18). Voltage measurements were performed before and after injecting water. Leak measurements are described in [17].

The electrode array consisted of 8 stainless steel electrodes, 20 cm long (1 unit), 1 cm in diameter, inserted 5 cm in the ground. The first electrode was placed at $x = –3.5$ and the eigth at $x = 3.5$. The electrode array was successively placed at $y = 2$, $y = 1$, $y = 0$, $y = –1$, $y = –2$, and $y = –3$, which constitutes the reference measurement whose aim is to eliminate the effect of the rocky layer on the reconstructed images.

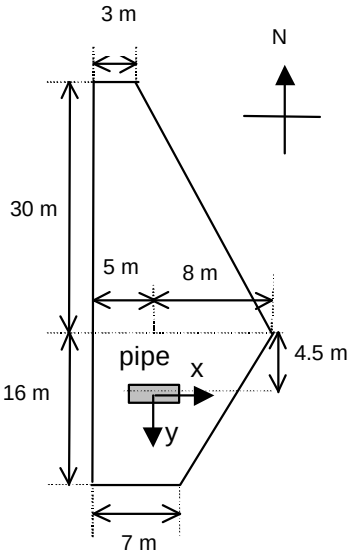

Figure 17: Field measurements layout. The 8 cm radius PVC tube was 1.06 m long and had been buried at 24 cm depth.

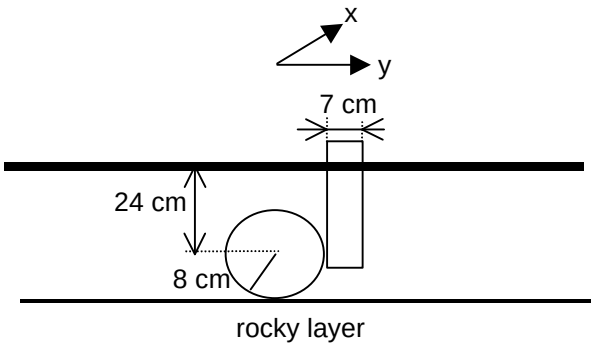

Figure 18: Buried tube and side tube used to simulate a water leak.

Figure 19 shows the 3D conductivity image obtained by using a $16 \times 5 \times 5$ grid of $1 \times 2 \times 0{,}5$ units voxels. The displayed conductivities are normalised to soil conductivity (about 0.01 S/m). The cross section at $y = 0$ (Figure 19a) shows a decreased conductivity in the central area close to the surface. The conductivity decrease in the shallower cells corresponds to the side tube in Figure 18. The reduced conductivity for voxels in the second and third rows correspond to the PVC tube. The horizontal cross-section through $z = 0.75$ (Figure 19b) reinforces the above conclusion because central voxels undergo a larger conductivity change. Conductivity changes in the south side may be due in part to the vertical tube.

a)

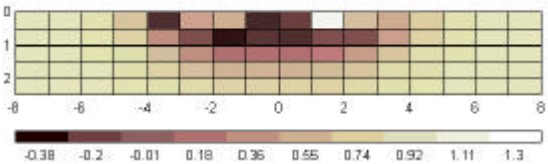

b)

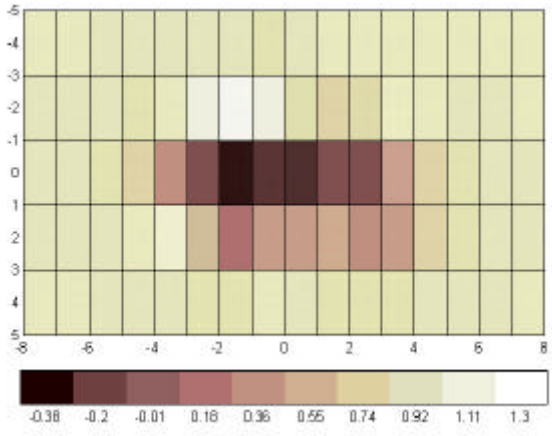

Figure 19: 3D image of a 8 cm (0.4 units) radius PVC cylinder parallel to the *x* axis and placed at *y* = 0 and 24 cm (1.2 units) deep. Voltage measurements were performed placing the 8-electrode array at *y* = 2, *y* = 1, *y* = 0, *y* = –1, *y* = –2, *y* = –3, which constitutes the reference measurement. a) Vertical cross-section at *y* = 0. b) Horizontal cross-section at *z* = 0.75. ($I = 6.97 \times 10^{-5}$)

6. CONCLUSIONS

A one-step least-squares algorithm based in the Marquardt-Levenburg method yields 2D and 3D images from underground conductivity distributions. An approximated analytical solution for the direct problem yields accurate, fast synthetic data for a spherical target. 3D solve the ambiguity resulting from different target positions yielding the same 2D image.

Experimental measurements using a water-filled plastic tank with immersed objects shows that images deteriorate for increasing sphere depth. Cylindrical targets whose axis is perpendicular to the electrode array can be described by a 2D cross section, which needs only a reduced number of voltage measurements.

Field measurements have allowed us to detect a plastic tube buried into a farm field and to validate the proposed algorithm. The effect of underlying ground layers is eliminated by first taking a reference measurement.

REFERENCES

[1] M. Noel and B. Xu, "*Archaeological investigation by electrical resistivity tomography: a preliminary study*", *Geophys. J. Int.*, 1991, **107**, pp. 95-102.

[2] R.H. Burger, "*Exploration geophysics of the shallow subsurface*". Englewood Cliffs (NJ): Prentice Hall, 1992.

[3] D.C. Barber and B.H. Brown, "*Applied potential tomography*", *J. Phys. E: Sci. Instrum.*, 1984, **17**, pp. 723-733.

[4] C. J. Kotre, "*Subsurface electrical impedance imaging using orthogonal linear electrode arrays*", *IEE Proc. Sci. Meas. Tech*, 1996, **143**, pp. 41-46.

[5] P. Tsourlos, J. Szymanski, J. Dittmer and G. Tsokas, "The use of weighted back-projection for fast inversion of vertical profiling resistivity data", *Proceedings of the 2nd congress of the hellenic geophysical union*, 5-7 May, 1993, Florina.

[6] M.H. Loke and R.D. Barker, "*Least-squares deconvolution of apparent resistivity pseudosections*", *Geophysics*, 1995, **60**, pp. 1682-1690.

[7] D.W. Oldenburg, P.R. McGillivray and R.G. Ellis. "*Generalized subspace methods for large-scale inverse problems*", *Geophys. J. Int.*, 1993, **114**, pp. 12-20.

[8] M.H. Loke and R.D. Barker, "Practical techniques for 3D resistivity surveys and data inversion", *Geophysical Prospecting*, 1996, **44**, pp. 499-523.

[9] M. Gasulla, J. Jordana and R. Pallás-Areny, "*Subsurface resistivity imaging using two single-step algorithms*", *IV Meeting of the Environmental and Engineering Geophysical Society*, September 14-17, 1998, Barcelona, pp. 291-294.

[10] L.R. Lines and S. Treitel, "*Tutorial. A review of least squares inversion and its application to geophysical problems*", *Geophysical prospecting*, 1984, **32**, pp. 159-186.

[11] M. Gasulla, J. Jordana and R. Pallás-Areny, "*Automated electrical impedance measuring systems to detect leaks from buried pipes*", *IV Meeting of the Environmental and Engineering Geophysical Society*, September 14-17, 1998, Barcelona.

[12] D.B. Geselowitz, "*An application of electrocardiographic lead theory to impedance pletysmography*", *IEEE Transactions on biomedical Engineering*, 1971, **18**, pp. 38-41.

[13] Wait, J.R. (1982) *Geo-electromagnetism*. New York: Academic Press.

[14] Telford, W.M.; Geldart, L.P.; Sheriff, R.E. (1990). *Applied Geophysics*. New York: Cambridge University Press.

[15] C. Hansen, "*Regularization Tools: A Matlab package for analysis and soluton of discrete ill-posed problems*", 1992, Danish computing Center for Research and Education, Technical University of Denmark.

[16] F.J. Llorens, "Automated system for soil resistivity measurement", PFC ETSETB, 1998. (In Catalan)

[17] J. Jordana, M. Gasulla and R. Pallás-Areny, "*Leakage detection in buried pipes by electric impedance imaging*", *1st World Congress on Industrial Process Tomography*, April 14-17, 1999, Buxton, UK.